ACS Sustainable Chemistry & Engineering

Research Article

pubs.acs.org/journal/ascecg

Graphene-Anchored Cuprous Oxide Nanoparticles from Waste Electric Cables for Electrochemical Sensing

S. M. Abdelbasir,*[,†] S. M. El-Sheikh,[†] V. L. Morgan,[‡] H. Schmidt,[‡] L. M. Casso-Hartmann,[§] D. C. Vanegas,[§] I. Velez-Torres,[∥] and E. S. McLamore*[,‡]

[†]Central Metallurgical Research and Development Institute, P.O. Box 87, Helwan, 11421 Cairo, Egypt

[‡]Agricultural & Biological Engineering, Institute of Food and Agricultural Sciences, University of Florida, 1741 Museum Road, Gainesville, Florida 32611, United States

[§]Food Engineering Department, and [∥]Environmental and Natural Resource Engineering, Universidad del Valle, Cali, Valle del Cauca, Colombia

Supporting Information

ABSTRACT: We demonstrate development of electrochemical nanosensors for planetary health applications using nanocuprous oxide synthesized from recycled materials. Laser-scribed graphene electrodes were enhanced with copper liberated from waste cables, and cuprous oxide nanospheres were synthesized via precipitation at low temperature using lactose as a reducing agent and four different surfactants as capping agents. These laser-scribed electrodes are a low-cost, lithography-free approach to direct synthesis of flexible carbon circuits. Sensors were fabricated by anchoring nanoparticles to flexible graphene electrodes, and then material properties and sensor performance were compared for each surfactant. Surfactant molecular weight and terminal group played an important role in nanoparticle size, band gap, ferromagnetic response, and electron transport. As proof of principle, we show development of catecholamine and mercury sensors for planetary health applications using the best material. Dopamine sensors were linear from 300 nM to 5 μM, with a detection limit of 200 nM, response time of 2.4 ± 0.7 s, and sensitivity of 30 nA μM cm^2. Mercury sensors were linear from 0.02 to 2.5 ppm, with a detection limit of 25 ppb, response time of <3 min, and sensitivity of 10 nA ppm^{-1}. The methods shown here are facile, environmentally friendly, and economical. Green synthesis of flexible sensors and electronic devices with recovered waste represents a sustainable approach for next-generation flexible carbon sensors for planetary health applications.

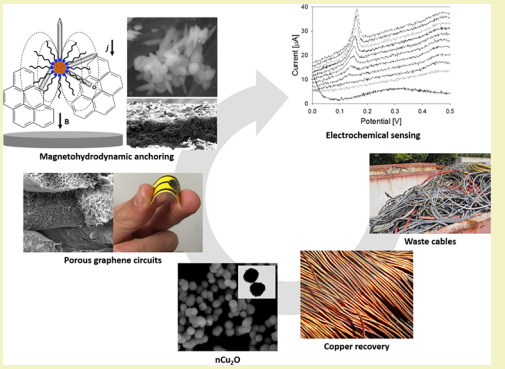

KEYWORDS: *Nanostructure, Cuprous oxide, Waste electric cable, Coprecipitation, Flexible sensor, Laser-induced graphene, Planetary health*

INTRODUCTION

There is a pressing need for low-cost, facile sensors that utilize green synthesis methods and recycled materials. Real-time point-of-need monitoring of environmental pollutants, agrochemicals, and medical biomarkers is critically important for planetary health.[1] For example, in several developing countries, mercury is a pollutant associated with artisanal gold mining and can occur in different chemical forms with varying levels of toxicity.[2] Acute exposure can lead to severe neurological, renal, or immune problems,[3] while chronic exposure leads to inactivation of catecholamine-0-methyl transferase, resulting in neurological dysfunction, increased blood pressure, gastrointestinal disturbances, and elevated urine catecholamines.[4] Other impacts are associated with environmental change that can negatively impact traditional livelihoods of local communities. Velez-Torres et al.[5] recently developed a model system for integrating analytical sciences and social sciences in mercury monitoring within artisanal gold mining communities. Given the economic importance of artisanal gold mining to many regions of the world, it is important to monitor and track the use of harsh chemicals such as mercury and their effects on species within the local ecosystem. In fact, the international Minamata convention calls for eradication of mercury, particularly in artisanal gold mining. To establish effective remediation and risk management strategies related to toxic compounds such as mercury, low-cost sensors are needed to monitor ecological samples (e.g., food, water) as well as exposure biomarkers in human fluids. Since use of mercury in artisanal mining primarily occurs in developing countries with limited resources,[5] low-cost and field-capable sensors are sorely needed. One of the biggest challenges in this context is to use abundant materials that require little or no preprocessing and/

Received: May 30, 2018
Revised: July 9, 2018
Published: August 14, 2018

DOI: 10.1021/acssuschemeng.8b02510
ACS Sustainable Chem. Eng. XXXX, XXX, XXX−XXX

or green synthesis methods, with the aim of avoiding planetary health problems related to sensor disposal.

In the past few decades there has been an explosion of graphene-based sensor platforms and common fabrication methods include the following: drop-cast coating,[6,7] inkjet printing,[8] and laser scribing/exfoliating,[9,10] among others. Laser-scribed graphene (LSG), also known as laser-induced graphene, has emerged as one of the most exciting sensor platforms due to the direct conversion of sp^3-hybridized carbon to sp^2-hybridized carbon, which is the allotrope found in graphene.[11] In LSG, laser ablation of polyimide (λ = 405 nm) induces lattice vibrations by locally increasing the temperature and breaking atom bonds of the polyimide chains, leading to atom recombination and gas production. Atomic rearrangement in aromatic compounds found within the polyimide results in few-layer porous graphene nanostructures.[12,13] LSG is a one-step lithography-free process for making porous graphene sensors at room temperature without the need for pretreatment.[14] Electrochemical graphene devices such as LSG sensors are commonly functionalized with metal nanostructures to increase transduction, including gold,[15] platinum,[16] palladium,[17] and copper.[18,19] Among these hybrid nanomaterials, copper–graphene hybrids are gaining traction due to the relatively high abundance of Cu^{2+} source material in addition to the opportunity to utilize recycled source material.[20,21]

While copper has great promise for synthesis of sensors, many applications are restricted due to the inherent instability of copper under atmospheric conditions. As discussed in the comprehensive review by Gawande et al.,[22] the biggest challenges are related to production of highly active, selective, stable, robust, and inexpensive nanostructured copper.[23] In the past decade, many groups have focused on core–shell nanoparticles or copper oxide/cuprous oxide (Cu_2O) nanoparticles, which are less susceptible to oxidation.[24] Numerous Cu_2O nanoparticles with varying crystallinity, particle size, and morphology have been synthesized using bottom-up (molecular assembly by atomic precursors) or top-down (physical/chemical size reduction) methods.

In bottom-up nCu_2O synthesis, nanoparticle morphology is controlled by altering physicochemical conditions, with copper salts as the base material and capping agents used to terminate particle growth. For example, monodisperse nanocubes were prepared by Guo and Murphy[25] by the reduction of Cu(II) salts in the presence of polyethylene glycol (PEG, mol. wt. 600 g/mol) and cetyltrimethylammonium chloride (CTAB) as protecting agents. CTAB-capped Cu_2O nanospheres have been synthesized with similar methods using hydrazine and organic additives as the reducing agent.[26] Submicrometer octahedrons have been synthesized using polyvinylpyrrolidone (PVP) as the capping agent[27] or with D-glucose and hydrazine as reducing agents.[28] Gawande et al.[22] provide a comprehensive review of other morphologies obtained with bottom-up fabrication. While bottom-up methods are efficient, there is an opportunity for synthesizing sustainable sensor materials by recycling copper from discarded electronics using top-down methods.

Top-down synthesis of nCu_2O from waste printed circuit boards was demonstrated by combining supercritical water (SCW) and electrokinetic (EK) techniques.[29] Uniform monodisperse Cu_2O nanospheres were prepared in the presence of PVP as a surface stabilizer, and the nanoparticle size could be tuned in the range of 18–50 nm by altering current density. Copper nanospheres (20–40 nm) have been produced with sublimation of copper wire using pulsed plasma discharge methods (5–6 kV).[30] Using copper flakes or microparticles as the starting material, a number of top-down methods can be used to synthesize nanoparticles ranging in size from 20 200 nm. For example, thermochemical reaction with 1-butyl-3-methylimidazolium ionic liquids, including tetrafluoroborate and hexafluorophosphate, can be used,[31,32] in addition to sonochemical synthesis[33] or laser irradiation[34,35] among other techniques. Limitations of these previous methods include need for toxic reagents, use of high sonication frequencies (high energy), creation of plasma (high energy), or need for mechanical size reduction to the micron scale prior to nanoparticle synthesis.

Here, we develop a simple, low-temperature (<125 °C), green process for synthesizing nanoscale Cu_2O particles from waste electric cables using top-down synthesis. The synthesis uses lactose as a reducing agent at room temperature, and we tested four different surfactants as capping agents to explore the best anchoring strategy for attaching nCu_2O to laser-induced graphene (LSG) electrodes. A magnetohydrodynamic anchoring method was developed for functionalizing porous graphene electrodes with the nCu_2O. As proof of concept applications, electrochemical sensors were demonstrated for measuring targets important to environmental pollution (mercury) and related medical diagnostics (dopamine).

EXPERIMENTAL SECTION

See the Supporting Information for details on materials and equipment.

Synthesis of Nanostructured Cuprous Oxide. Primary treatment of waste electronic cables (WECs) for removing insulating material was conducted in a three-neck flask fitted with a reflux tube, thermometer, and separating funnel containing DMSO. An electroheating mantel was used to control temperature at 125 °C (see Supporting Information Figure S1). WECs were cut into 3 cm long pieces, then submerged into DMSO (total concentration of 5% w/v), and then maintained at 125 °C for 3 h in the electroheating mantel. Aliquots (2 g) of the recovered Cu wire were dissolved in 100 mL of 4 M aqueous H_2SO_4 solution with 1 mL of 1% H_2O_2 (v/v) added to enhance dissolution. Next, 0.2 g of surfactant, either CTAB, polyethylene glycol (PEG_{4000}), $Brij_{56}$, or Pluronic (P_{123}), was separately added, and the solution was stirred for 3 h at 125 °C. The solution pH was adjusted to 11 using NaOH, and then 10 mL of lactose (2.92 M) was added while the solution was stirred vigorously for 30 min at room temperature. The Cu_2O particles were coprecipitated in a flask under ambient conditions, filtered with 0.45 μm cellulose acetate filter paper (Whatman), washed with distilled water, washed in absolute ethanol, and finally dried at 60 °C for 3 h on a crucible.

Material Characterization and Imaging. The phase identification, relative crystallinity, and crystallite diameter (i.e., Scherrer size) of prepared nanoparticles were analyzed with X-ray diffraction (XRD, Bruker AXS-D8, Germany) using Cu–Kα (λ = 1.5406 Å) with a secondary monochromator. Infrared (IR) spectra were obtained with an FT-IR spectrometer using KBr tablets (JASCO 3600) from 400 to 4000 cm^{-1}. Magnetic properties were analyzed using a vibrating sample magnetometer (7400-1 VSM, U.S., Lake Shore Co., Ltd., USA) in a maximum applied field of 20 kOe. Photoluminescence spectroscopy was analyzed using an RF-5301 instrument with spectrum type EM at a scan range of 220–900 nm. UV–vis spectroscopy (reflectance spectra) was analyzed using a Varian Cary 100 Scan UV–vis system equipped with a Lab-sphere integrating sphere diffuse reflectance accessory at wavelengths from 190 to 2200 nm using $BaSO_4$ as a reference material. Absorption coefficients were calculated from reflectance data according to the equation $R = \{(1 - R)^2/2R\}$. Optical band gap was calculated using the Tauc relationship[36–38] according to eq 1. The linear region of the Tauc plot

DOI: 10.1021/acssuschemeng.8b02510
ACS Sustainable Chem. Eng. XXXX, XXX, XXX–XXX

indicates the band gap of the Cu_2O sample, which was used to estimate absorption edge energies for each material.

$$\alpha \times h\nu = -(h\nu - E_g)^n \quad (1)$$

where $h\nu$ is the photon energy, E_g is the band gap energy, α is molar extinction coefficient, and n is the constant exponent that determines the type of optical transition.

Morphology was characterized using field emission scanning electron microscopy (FE-SEM; QUANTAFEG 250, Netherlands) and transmission electron microscopy (TEM) with an acceleration voltage of 200 kV, magnification power of 600 k×, and resolution of 0.2 nm (TEM, JEOL-JEM-1230, Tokyo, Japan). Photographs of LSG sensors were taken with a Nikon camera, and SEM images of sensors were taken on a JEOL 5600 LV, with accelerating voltage of 12−15 kV based on our previous work.[39−41]

Flexible LSG−nCu$_2$O Sensor Fabrication. Electrodes were fabricated on polymer/cellulose substrate based on work by Tehrani and Bavarian[42] and Fenzl et al.,[43] with minor modifications. Electrodes were fabricated as described by our recent work[44] using pulsed UV laser irradiation of a polyimide/cellulose composite prepared by adhering polyimide tape (aka Kapton tape) to the gelatin emulsion side of the photopaper. A 405 nm laser (1 W) with two-dimensional stepper motors was used to pattern the electrodes using a laser pulse rate of 30 ms (laser energy density of 2.3 J cm^{-2}). After the LSG surface (approximately 60 μm thick) was formed, the reference electrode was coated with Ag/AgCl ink (approximately 60 μm thick), and then the wires were passivated using a nitrocellulose lacquer layer (approximately 200 μm thick) (see Supporting Information Figure S2).

Prepared nCu$_2$O were anchored to the graphene surface using magnet-assisted electrodeposition based on a modified version of Fattahi and Bahrololoom.[45] A solution of nCu$_2$O solution was prepared by adding 150 mg of nCu$_2$O powder to 500 μL of DMSO followed by vortex mixing for 1 min. The solution was then then diluted (1:2) with 70% ethanol , and 10 mM Cu_2SO_4 was mixed into the solution to seed crystal growth during anchoring. A 100 μL aliquot was drop cast on the working electrode, and the LSG sensor was placed directly over a neodymium magnet (perpendicular magnetic field) for anchoring of the nCu$_2$O by magneto-hydrodynamic (MHD) electrodeposition. A copper mesh (0.5 mm diameter) was immersed in the liquid and connected to the cathode of the power supply while the LSG working electrode was connected to the anode. Pulsed electrostatic deposition at 67 mHz, total plating time of 60 s at 10 V, was used to anchor the copper nanoparticles to the LSG.[41] Prior to use, the copper mesh was polished for 30 s at 10 V in a solution of 25% ethanol and 25% phosphoric acid. After nCu$_2$O anchoring, LSG electrodes were rinsed with DI water and allowed to dry at room temperature prior to use.

Baseline Electrochemical Testing of LSG−nCu$_2$O. Electrochemical characterization was performed using a three-electrode cell stand (C-3, BASi, West Lafayette, IN) as previously described.[39] Cyclic voltammetry was carried out in 4 mM $Fe(CN)_6$/1 M KNO_3 solution at a switching potential of 800 mV. Where noted, a commercial reference electrode (RE-5B, BASi, West Lafayette, IN) and platinum wire were used for testing of LSG working electrodes functionalized with nCu$_2$O for comparison. Electroactive surface area (ESA) and heterogeneous electron transfer constant (k_s) were determined using the Randles−Sevcik theorem as described in previous work[39,46] (see Supporting Information for details on calculation of k_s).

Proof of Concept Electrochemical Sensors. For catecholamine sensing, a Nafion layer was first applied to the nCu$_2$O−LSG working electrode following the procedures in Chaturvedi et al.[47] DC potential amperometry (DCPA) was conducted in 250 mM PBS (pH 7.0) at room temperature using a working potential of +100 mV (sampling rate of 1 kHz) based on Sotomayor et al.[48] After 30 min of polarization, the current output was measured while successively injecting dopamine in the stirred working solution (450 rpm) at 5 min intervals. DCPA time series were used to evaluate the performance of the sensor (sensitivity, response time, and lower limit of detection) based on Vanegas et al.[39]

Mercury sensors were tested using linear sweep stripping voltammetry (LSSV) in a 100 mM hydrochloric acid (HCl) solution based on a procedure modified from Dai and Compton.[49] In summary, LSSV was performed from −800 to 1600 mV at a deposition time of 100 s, quite time of 5 s, and a scan rate of 20 mV/s. An Ag/AgCl electrode was used as the reference electrode, a platinum wire as the counter electrode, and a nCu$_2$O−LSG electrode as the working electrode.

Statistical Analysis. A completely randomized design was used to evaluate the effect of the capping agent on the surface properties and electrochemical performance of nanocopper-modified graphene electrodes. All sensor experiments were performed in triplicate, and results are expressed as arithmetic mean ± standard deviation. One-way ANOVA was performed to establish any significant differences among treatments ($p \leq 0.05$).

RESULTS AND DISCUSSION

Material Characterization of nCu$_2$O Powders. Morphology and size of nCu$_2$O powders capped with different agents (CTAB, Brij$_{56}$, PEG$_{4000}$, P$_{123}$) were examined by SEM and TEM (Figure 1). Nuclei were assembled through reduction of Cu^{2+} ions by lactose, resulting in metastable spheres composed of nanocrystals and amorphous domains, where the molecular weight of the capping agent and type of terminal group played a crucial role in particle size and morphology. FE-SEM (left side of Figure 1) shows that

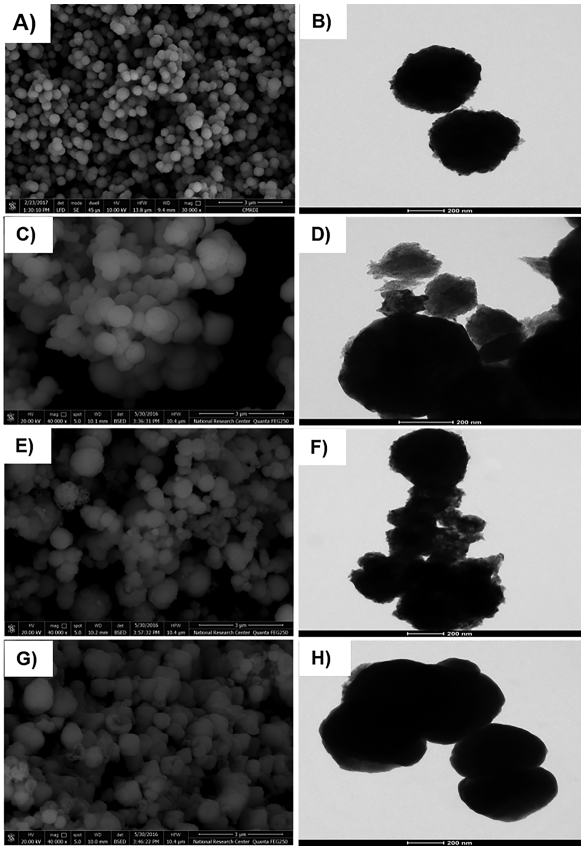

Figure 1. Electron microscope images of nCu$_2$O prepared with various surfactants. Scale bars for FE-SEM images (left) are 1 μm; scale bars for TEM images (right) are 200 nm. (A, B) CTAB; (C, D) Brij$_{56}$; (E, F) PEG$_{4000}$; (G, H) P-123. Additional high-resolution TEM images can be found in the Supporting Information.

DOI: 10.1021/acssuschemeng.8b02510
ACS Sustainable Chem. Eng. XXXX, XXX, XXX−XXX

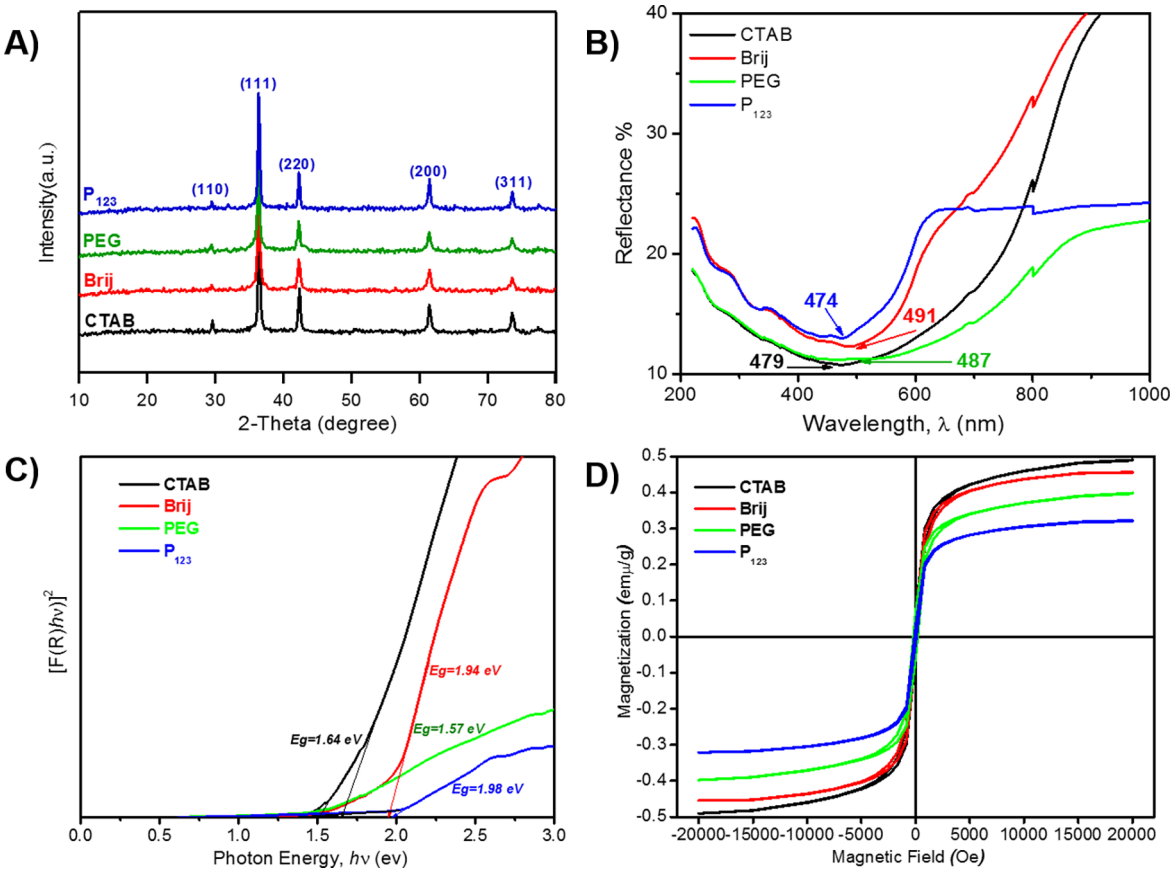

Figure 2. Material characterization of nCu_2O powders prepared by dissolution with 4 M sulfuric acid concentration using different capping agents. (A) XRD patterns show five sharp peaks indexed to a single phase of crystalline Cu_2O. (B) UV−vis spectra show different diffuse reflectant peaks (indicated on figure). (C) Tauc plots showing optical band gap for each powder (value indicated on figure). (D) Magnetic properties of each nCu_2O powder at room temperature.

particles have a spheroid morphology with narrow particle size distribution and a relatively smooth surface; TEM images are shown on the right side of Figure 1. Nanoparticle capping with CTAB (Figure 1A, B) yielded uniform, dispersed mesospheres approximately 200−250 nm in diameter. $Brij_{56}$-capped nanoparticle powders (Figure 1 C, D) consisted of a mixture of relatively large 200−400 nm nanospheres and smaller 50−100 nm mesospheres. These mesospherical morphologies are due to Oswalt ripening, where smaller Cu_2O nanoparticles act as a catalytic center for the formation of larger structures, ultimately leading to mesospheres of varying size.[50] PEG_{4000}-capped nanoparticle powders (Figure 1 E, F) contained mesospheric 180−220 nm structures as well as amorphous nanoparticles (see Supporting Information Figures S3−S4), while P_{123}-capped particles (Figure 1 G, H) consisted of monodisperse 300 nm spheres with a smooth surface. Interior holes/voids appear within each of the solid nanospheres, which is likely due to formation of relatively large static crystallites as a result of dissolution and recrystallization of smaller crystals.

Figure 2A shows XRD patterns of the produced nCu_2O powders with various capping agents. For each material, five sharp peaks were indexed to a single phase of crystalline Cu_2O according to JCPDS No. 75-1531. The 2θ value associated with Cu_2O peaks and corresponding crystal plane were the following: 29.6° (1 1 0), 37.7° (1 1 1), 43.7° (2 0 0), 62.8° (2 2 0), and 75.0° (3 1 1). The average crystallite size calculated for each sample using the Scherrer equation ranged between 20 and 42 nm. During early stages of formation, these Cu_2O crystallites are highly reactive because of the high interfacial energy. This causes nanocrystals to aggregate and form larger particles through attachment at high-index planes, creating nCu_2O with excellent electrochemical properties;[51] see Supporting Information Figure S5 and related text for a detailed discussion. No peaks associated with impurities were observed in any of the powder samples.

Figure 2B shows the UV−vis reflectance spectra of nCu_2O powders. Reflectance peaks for each material were similar, CTAB (479 nm), $Brij_{56}$ (491 nm), PEG_{4000} (487 nm), and P_{123} (474 nm), but lower than that of bulk Cu_2O (570 nm, band gap ~2.17 eV),[36] which is attributed to the varying size of nCu_2O as described by Yuan et al.[52] The surface plasmon resonance value was located near the broad absorption peak from 257 to 503 nm when using PEG_{4000}, likely resulting from the inhomogeneous size of the nanoparticles.[53] The peak position for P_{123}-capped particles was blue-shifted by approximately 15 nm relative to $Brij_{56}$-capped particles. This shift corroborates with particle size analysis by TEM since stronger shifts occur as particle size decreases, as predicted by Mie theory.[54] Peaks for CTAB- and PEG_{4000}-capped nanoparticles were also red-shifted due to the homogeneous size of the nCu_2O. The Tauc relationship was used to calculate optical band gap for each nanoparticle (Figure 2B). Representative edge energies were CTAB (1.64 eV), $Brij_{56}$ (1.94 eV), PEG_{4000} (1.57 eV), and P_{123} (1.98 eV). The band gaps for $Brij_{56}$- and P_{123}-capped nanoparticles were close to the direct band gap of bulk Cu_2O (2.0−2.17 eV), while CTAB- or PEG_{4000}-capped

DOI: 10.1021/acssuschemeng.8b02510
ACS Sustainable Chem. Eng. XXXX, XXX, XXX−XXX

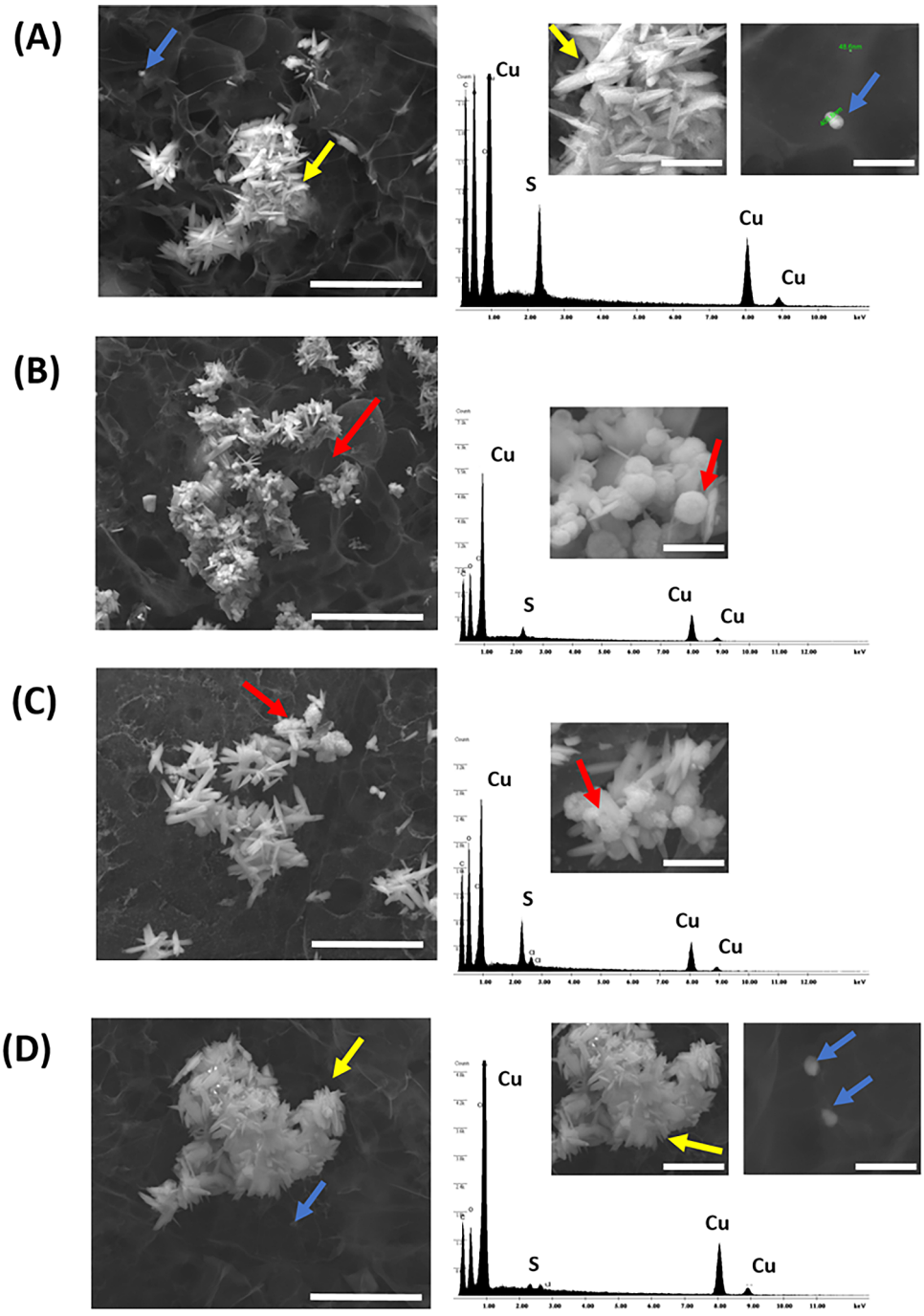

Figure 3. SEM (left) and EDS (right) for LSG metallized with nCu_2O particles for each type of capping agent: (A) CTAB, (B) $Brij_{56}$, (C) PEG_{4000}, and (D) P_{123}. Scale bars for images on the left are 10 μm; scale bars for insets on the right are 10 μm. Blue arrows indicate isolated nCu_2O not anchored to LSG; yellow arrows indicate isolated copper crystals not associated with nCu_2O spheres; red arrows show urchin-like nanostructures anchored to graphene by Cu crystals. EDS spectra indicate peaks associated with Cu and S. EDS for isolated nCu_2O are shown in Supporting Information Figure S11.

nanoparticles had relatively low edge energies. The band gap decreased with particle size due to quantum confinement, which has also been shown for other similar cuprous oxide nanoparticles.[50]

Room temperature photoluminescence (PL) spectra (Figure 2C) showed strong visible emission bands in the range of 757−754 nm, corresponding to a band gap of 1.60−1.98 eV, which confirms trends observed for reemission spectra in Figure 2B. The broadening of the peak as compared to bulk Cu_2O is a function of the relatively small crystallite size for the nanoparticles. Interestingly, $Brij_{56}$-capped nanoparticles (spheroids) and P_{123}-capped nanoparticles (hollow spheres) showed significantly higher PL intensity relative to CTAB-capped particles (uniform rough microspheres) and PEG_{4000}-capped particles (amorphous spheres). High-resolution TEM images of CTAB- and PEG_{4000}-capped particles are shown in Supporting Information Figures S5−S8. The outer surface of these microspheres was rough in nature, suggesting that the spheres are composed of single crystalline nanoparticles.[51] This difference in PL intensity is attributed to the difference in size/

DOI: 10.1021/acssuschemeng.8b02510
ACS Sustainable Chem. Eng. XXXX, XXX, XXX−XXX

morphology and density of defect sites. The luminescent band at ~755 nm is attributed to the presence of oxygen vacancies (VO band) with a high defect density, resulting in an almost invisible exciton emission near the Cu_2O band gap region as reported by others.[55−57] Since Cu_2O nanospheres capped with $Brij_{56}$ or P_{123} had a higher PL intensity when compared to nanoparticles capped with CTAB or PEG_{4000}, this suggests an enhanced density of defects that is assigned to recombination centers.

Room temperature magnetization for each surfactant-capped Cu_2O sample in a magnetic field (M−H) loop is shown in Figure 2D. Magnetizations of nanoparticles capped with CTAB (0.49 emu/g) and $Brij_{56}$ (0.46 emu/g) were higher than particles capped with PEG_{4000} (0.40 emu/g) and P_{123} (0.32 emu/g). The coercive field was highest for particles capped with PEG_{4000} (192 G), lowest for P_{123} (87 G), and moderate for CTAB (135 G) and $Brij_{56}$ (130 G). The trend in ferromagnetic characteristics is likely a size effect due to varying surface magnetic anisotropic energy gap[58] and also the presence of vacancy crystal defects.[59] The limited-size effects and vacancy concentration on the nanoparticle surface are the probable reasons for these paramagnetic and diamagnetic properties. On the other hand, it is conceivable that this may be a result of oxygen/cation vacancies which is in good agreement with PL data. Pure Cu_2O with an ideal lattice structure is diamagnetic since the d shell of Cu^{1+} is complete, i.e., the electron configuration of Cu^{1+} is 3d,[10] and neither Cu^{1+} nor O^{2-} is a magnetic ion. The origin of magnetism may not arise from the copper atom 3d electrons but rather from unpaired 2p electrons of oxygen atoms in the immediate vicinity of the cation vacancies.[60−62]

Based on the properties described above, flexible laser scribed graphene (LSG) sensors were fabricated by anchoring nCu_2O to graphene surfaces using magnetohydrodynamic (MHD) electrodeposition. General characterization of the LSG−nCu_2O material was conducted using SEM and EDS, and then baseline electrochemistry was analyzed using CV and EIS. For each nanoparticle type, electrochemical sensors were tested for measurement of small molecules (dopamine or mercury) as a proof of concept.

nCu_2O Anchoring on Graphene Electrodes. Prior to metallization, LSG show a stitched microscale pattern that results from laser rastering across the polymer surface during graphitization (see Supporting Information Figure S9). The exposed nanostructures are rich in edge structures, which is a graphitic feature with high chemical reactivity.[63,64] In preliminary anchoring experiments, nCu_2O electrodeposited in the absence of a magnet field was unstable during electrochemical measurements (see Supporting Information Figure S10). To improve anchoring, we first attempted to use sonoelectrodeposition for cavitating bubbles based on Taguchi et al.[41] and also tested various magnet arrangements for MHD. The optimal results for nCu_2O anchoring on LSG were obtained for a perpendicular magnetic field of 1 T and no sonication. Figure 3 shows representative SEM and EDS for each type of capping agent.

LSG electrodes metallized with CTAB-capped nCu_2O (Figure 3A) or P_{123}-capped nCu_2O (Figure 3D) contained many large copper spinelike structures formed during electrodeposition (yellow arrows), but these were not associated with the 50−500 nm nCu_2O spheroids in any of the samples analyzed (see also Supporting Information Figure S11). All of the nCu_2O in SEM images for CTAB-capped or P_{123}-capped particles was isolated as shown in Figure 3A and Figure 3D (blue arrows). EDS confirmed both Cu and S were present in the crystals, but the isolated nCu_2O contained no sulfur, confirming that the anchoring mechanism was not effective for this type of capped nanoparticle; trace S is a key indicator of the anchoring mechanism since urchin-like nanostructures are only formed during codeposition of Cu crystals and nCu_2O onto LSG. Among the capping agents used, these two nCu_2O were approximately the same size (50−100 mesospheres with 200−300 nm larger spheres) but had different molecular weights and terminal groups. CTAB is a cationic surfactant (MW 365 g/mol) terminated with a CH_3 group on the hydrophobic tail, while P_{123} is a nonionic surfactant (MW 5800 g/mol) with a terminal H group. On the other hand, LSG metallized with $Brij_{56}$-capped particles (Figure 3B) or PEG_{4000}-capped particles (Figure 3C) contained urchin-like structures, with clusters of nCu_2O spheroids that were anchored by Cu crystals (red arrows). In all the $Brij_{56}$ and PEG_{4000} samples analyzed, less than 4% of the nCu_2O was isolated from crystals formed during anchoring. EDS confirmed both Cu and S were present in the nano urchin structures, validating that the anchoring mechanism on LSG was highly efficient. $Brij_{56}$ is a nonionic surfactant (MW 682 g/mol) terminated with a CH_3 group, and PEG_{4000} is a cationic surfactant (MW 4000 g/mol) terminated with a H group, which produced mixtures of rough mesospherical nanoparticles that anchored to LSG. The unique mesospherical morphology contained abundant crystalline imperfection and grain boundary, leading to the formation of urchin-like structures. It is important to note that these urchin-like structures do not typically form in Cu electrodeposition,[65] but in this case the morphology was created by a two-step codeposition process; first nanospheres were prepared, and second the spheres were anchored to LSG. Nanourchin structures are known to significantly improve electrochemical performance due to improved interfacial contact between nanometal and underlying sp^2 carbon, as well as high surface area to volume ratio.[66,67]

Although the magnetic field and coercive force for the nCu_2O are relatively weak (0.3−0.5 emu/g and 160−220 G, respectively), MHD electrodeposition enhanced anchoring of the $Brij_{56}$- and PEG_{4000}-capped nanoparticles as shown in Figure 3. MHD is known to induce mixing in the electrical double layer resulting from interactions of the Lorentz force with the local current density, in turn reducing the diffusion layer thickness and enhancing mass transport. As described in the following sections, formation of the nanourchin structures shown in Figure 3B, C is vital to sensor performance for small-molecule sensing.

Zhou et al.[68] have shown that silver crystals can be used to anchor silver nanoparticles, but our work is the first to report a similar effect with nanocopper on graphene. Copper nanoparticles have been anchored to activated carbon or graphite using techniques such as adsorption or reflux chemistry.[69,70] Carbon nanotube/copper host/guest systems have been a major focus due to the ability to incorporate copper nanoparticles on the surface of the tube as well as within tubes.[71] Graphene-anchored copper nanoparticle hybrids have been synthesized by coreduction[72] and electrodeposition,[73] but this work is the first demonstration of MHD-anchoring of nanoparticles on graphene.

Electrochemical Analysis of LSG−nCu_2O. LSG sensors fabricated with anchored nCu_2O ($Brij_{56}$- and PEG_{4000}-capped particles) displayed distinct oxidation and reduction peaks at

DOI: 10.1021/acssuschemeng.8b02510
ACS Sustainable Chem. Eng. XXXX, XXX, XXX−XXX

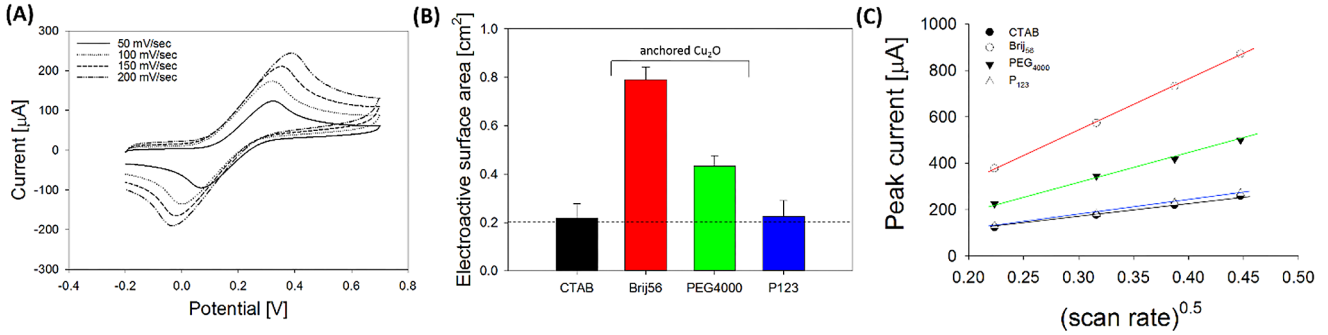

Figure 4. Electrochemical analysis of nCu_2O-coated LSG electrodes for each capping agent. (A) Representative cyclic voltammograms for $Brij_{56}$-coated nCu_2O on LSG for 4 mM KFeCN at room temperature. (B) Average electroactive surface area (ESA) for each nCu_2O-coated LSG electrode. The dashed line indicates the ESA of LSG electrodes functionalized with Cu by electrodeposition (0.21 ± 0.04 cm^2). The ESA for a bare LSG electrode (not shown) was 0.05 ± 0.01 cm^2. (C) Linear Cottrell plots are indicative of diffusion-limited transport.

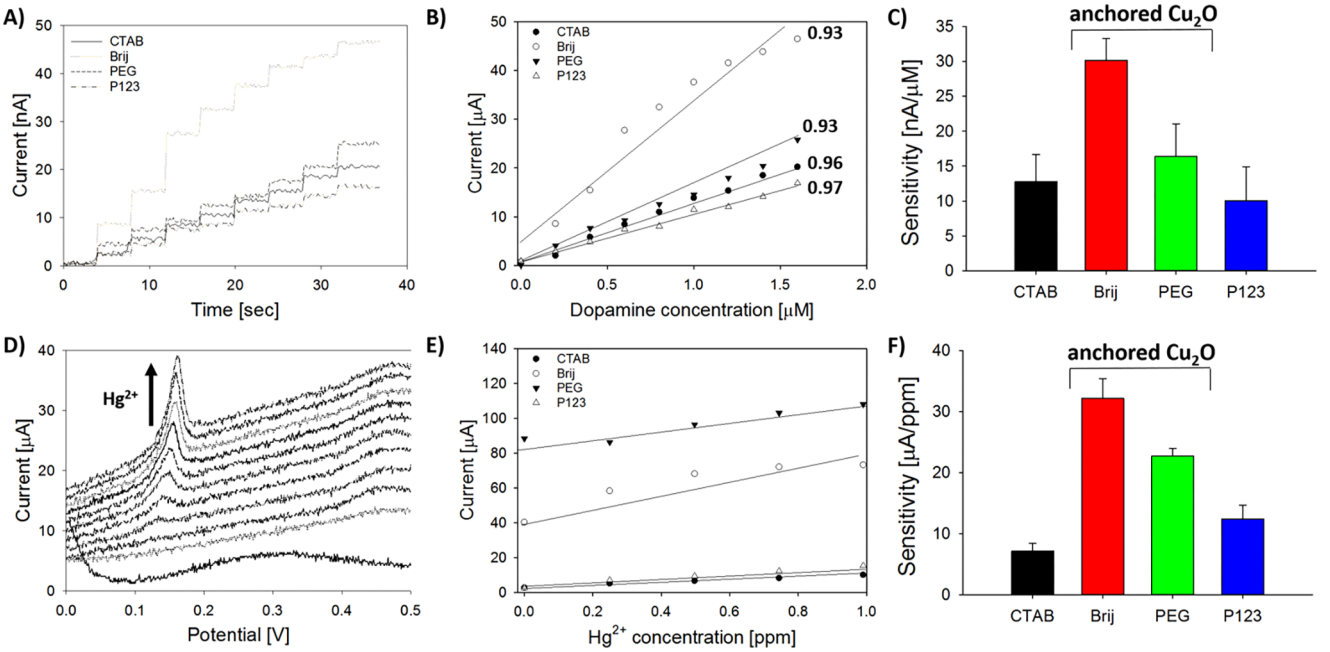

Figure 5. LSG sensors with graphene-anchored nCu_2O for nanoparticles prepared with each capping agent. (A) Representative DCPA plots during successive addition of dopamine at an oxidative potential of +400 mV. (B) Calibration plots for dopamine sensors. (C) Average sensitivity toward dopamine for sensors with different nCu2O capping agents. (D) Representative LSSV plots during successive addition of Hg^{2+}. (E) Calibration plots for Hg^{2+} sensors. (F) Average sensitivity toward Hg^{2+} for sensors with different nCu2O capping agents. All error bars represent standard deviation of the arithmetic mean. All correlation coefficients were higher than 0.93 for linear curve fitting (see Supporting Information section for details).

all scan rates tested (50−200 mV/s). Figure 4A shows representative CVs for $Brij_{56}$-capped anchored particles; CVs for other nanoparticles can be seen in Supporting Information Figure S12. The peak potential is similar to the Cu nanocubes formed on LSG by Tehrani and Bavarian,[42] although in our case the Cu_2O is available for nonreversible chemistry at −600 mV where in the case of the nanocubes a single reduction peak from ferricyanide was measured. As shown in Figure 4B, the electroactive surface area (ESA) for anchored nCu_2O was significantly higher than for nonanchored nCu_2O ($p < 0.005$, $\alpha = 0.005$). The peak current and ESA for electrodes with anchored $Brij_{56}$-capped particles (ESA = 0.84 ± 0.08 cm^2) was two to four times higher than for the other nCu_2O-coated electrodes. In addition, the heterogeneous electron transfer coefficient (k_o) for $Brij_{56}$-capped Cu_2O anchored to graphene (0.0007 cm/s) was 20−25% higher than for the other electrodes, which exceeds the values reported for edge-plane and basal-plane pyrolytic graphite.[43] Cottrell plots (Figure 4C) were linear at all scan rates tested, indicating diffusion-limited transport for all electrodes.

Figures 3−4 confirm the material analysis data in Figures 1−2 and show that anchored nCu_2O are an excellent transducer for electrochemical sensor applications. In the next sections, we demonstrate this concept by developing two different sensors for small molecules. The first sensor is based on amperometric oxidation of a model catecholamine (dopamine), and the second sensor is based on linear sweep stripping voltammetry measurement of mercury.

Demonstration of LSG−nCu_2O Sensing. DC potential chronoamperometry plots (E = +400 mV versus Ag/AgCl) demonstrate rapid oxidation of dopamine for sensors coated with each nCu_2O material (Figure 5A). The linear range for all sensors was from approximately 200 nM to 1.5 μM for all sensors (Figure 5B); all correlation coefficients for calibration

DOI: 10.1021/acssuschemeng.8b02510
ACS Sustainable Chem. Eng. XXXX, XXX, XXX−XXX

Table 1. Comparison of Performance Characteristics for Recent Dopamine and Mercury Electrochemical Sensors Composed of Copper-Modified Carbon Electrodes

analyte	platform[a]	sensitivity	limit of detection (μM)	linear range	response time	ref
dopamine	LSG−nCu_2O	85 μA mM^{-1} cm^{-2}	0.2	0.2−1.6 μM	2 s	this work
	3D SWNT−Ppy−tryosinase	477 μA mM^{-1} cm^{-2}	5.0	5−400 μM	5 s	76
	GCE−guar gum/tyrosinase	13 μA mM^{-1} cm^{-2}	0.1	2−10 μM	60 s	77
	carbon fiber coated with chitosan/tyrosinase	14 μA mM^{-1} cm^{-2}	1.1	10−220 μM	8 s	78
mercury	LSG−nCu_2O	178 nA ppm^{-1} cm^{-2}	25	50−2500 ppb	105 s	this work
	copper−cobalt GCE with CysH	289 nA ppm^{-1} cm^{-2}	16	50−500 ppb	600 s	79
	copper boron-doped diamond	165 nA ppm^{-1} cm^{-2}	0.04	0.1−30 ppb	225 s	80
	copper-modified gold electrode with invertase	40% ppb^{-1} cm^{-2}[b]	0.05[b]	10−55 ppb	15 min	81

[a]3D SWNT: Three-dimensional single-walled carbon nanotube matrix; Ppy: polypropylene; GCE: glassy carbon electrode; CysH: L-cysteine. [b]Phenylmercury measured with enzyme inhibition mechanism (reported as % inhibition).

cures were 0.93; see the Supporting Information section for details. The average response time (t_{95}) did not change significantly (2.4 ± 0.4 s) within the range tested. The average sensitivity (Figure 5C) was highest for anchored nCu_2O, which is consistent with baseline electrochemistry data shown in Figure 4. The limit of detection followed the same trend as sensitivity, where LSG prepared with anchored nCu_2O was significantly lower ($p < 0.001$). The sensitivity for sensors prepared with $Brij_{56}$-capped nCu_2O (30.2 ± 3.1 nA/μM) was at least twice as high as for the other sensors, which is consistent with the data in Figures 1−4.

Figure 5D shows a representative plot of Hg^{2+} sensitivity in 1 M HCl at room temperature for $Brij_{56}$-capped nCu_2O anchored to LSG, and calibration plots for all materials are shown in Figure 5E. All sensors were linear from 0.02 to 2.5 ppm with a response time of <3 min. The sensitivity for LSG nanosensors with $Brij_{56}$-capped nCu_2O (32 ± 3 μA/ppm) was significantly higher than for other sensors ($p < 0.001$, $\alpha = 0.05$; ANOVA) in the range of 0−1 ppm, and the LOD for these sensors was 25 ppb. The average sensitivity (Figure 5F) followed the same trends as previously described, where LSG prepared with anchored nCu_2O were more efficient than nonanchored n$C_{u2}O$.

The electrochemical sensors in Figure 5 depend on electron transfer reactions at defect sites, graphene edge/plane structures, and nCu_2O interior/exterior surfaces. Therefore, intimate contact between the nanometal and underlying graphene surface is of upmost importance to sensor efficacy. Sotomayor et al.[48] developed a biomimetic copper-based sensor for measuring dopamine by using bis(2,29-bipyridil) copper(II) chloride complex, a structure similar to that found in the active site of tyrosinase. Mercury sensors have been prepared on flexible graphene electrodes using aptamers as the biorecognition structure, with detection limits as low as 10 pM.[68] Although the long-term fate of the nCu_2O was not studied here, the polyimide base structure used for sensor fabrication is biodegradable by fungal biofilms,[74,75] indicating that the approach here is a viable option for creating sensors for using green/sustainable materials.

Table 1 shows a comparison of performance characteristics for recent dopamine and mercury electrochemical sensors composed of carbon electrodes (sensors modified with copper were included where possible). To date there are no reports of hybrid copper−carbon sensors that are based on sustainable materials (such as recovered e-waste), but Table 1 provides a comparison to recent published manuscripts which are similar.

For dopamine sensing, the LSG−nCu_2O electrode was comparable to, or better than, most hybrid copper−carbon sensors in the current literature. The sensitivity of a 3D SWNT−Py−tryosinase biosensor by Min et al.[76] was higher than the value reported here, but the LOD, linear range, and response time were superior for the LSG−nCu_2O. Furthermore, the 3D SWNT−Py−tryosinase used an enzyme immobilized in a complicated 3D SWNT matrix (the reproducibility of the 3D SWNT material was not reported, and the synthesis required harsh chemicals for synthesis). The LOD of a GCE−tyrosinase biosensor (enzyme immobilized in Guar gum) was slightly lower than the device herein,[77] but the remaining sensor performance characteristics in Table 1 were relatively poor, and the biosensor required use of an enzyme, which is often not possible in low resource applications such as artisanal gold mining. The carbon fiber electrode by Niagi et al.[78] had a wide operating range, but the LOD was relatively high and the sensitivity was much lower than the LSG electrode herein.

For mercury sensing, the LSG−nCu_2O sensor had a comparable sensitivity and improved response time/range over other copper−carbon hybrid sensors. Sharma et al.[79] developed a copper/cobalt-decorated glassy carbon electrode (GCE) modified with L-cysteine that had a higher sensitivity, but the sensor was not based on sustainable or green synthesis methods and reproducibility was not reported. Additionally, the LSG−nCu_2O device developed here has a wider range and a faster response time, which are critical features for field analysis. Chaiyo et al. (2014) developed a copper/boron-doped diamond electrode with an excellent LOD (0.04 μM), but the sensitivity and range were relatively low. Additionally, the synthesis methods are relatively complex, limiting the sustainable production during scale up. Mohammadi et al. (2004) developed a biosensor based on copper-modified gold electrodes coated with invertase. Enzyme inhibition was monitored by recording amperometric oxidation of sugars in the presence of phenylmercury. While the approach is not applicable for field applications such as artisanal gold mining (due to the fragile nature of invertase), this manuscript provides a first step in the on-site detection of methylmercury with electrochemical copper sensors, an important area of research since methylmercury is significantly more toxic than ionic mercury.

Although we focus on development of sensors in this work, graphene−metal hybrids have a long list of other applications, including super capacitors and batteries,[82] flexible electronics,[83] and electrocatalysts,[84] and many other applications as reviewed by Daniele et al.[18] Realizing the useful properties of graphene is generally limited since most procedures rely on complex fabrication procedures that require multiple process-

DOI: 10.1021/acssuschemeng.8b02510
ACS Sustainable Chem. Eng. XXXX, XXX, XXX−XXX

ing steps (thermal annealing, mask lift off, etc.). The methodologies here are low cost and simple and extend to other protocols for graphene-based electrical devices such as inkjet printing,[8,85] screen printing,[86] or dispenser printing,[87] among others.

CONCLUSION

The metal recovery and sensor fabrication methods shown here are facile, environmentally friendly, and economical. Green synthesis of flexible sensors and other electronic devices with recovered electronic waste is an important area of research for the growing nanomanufacturing industry, as resource availability and environmental sustainability are becoming increasingly important in the design and application of electronic devices such as sensors. This work represents a new advancement in development of electrochemical sensors for planetary health applications and can be recreated in any basic laboratory using wet chemistry techniques and a low-cost laser engraver. The approach herein is scalable, as electric cables are widely used in transportation, construction, communication, and consumer commodities. This work is the first to report preparation of flexible graphene electrodes incorporating waste materials, and the sensors were demonstrated for monitoring environmental and/or medical fluids related to mercury exposure. In contrast to conventional spherical nanoparticles, the unique mesospherical morphology of the Cu_2O nanoparticles here produces highly stable, linker-free, and size tunable structures which can be easily anchored to graphene. The observed enhanced electrochemical performance was related to nCu2O structure, where anchoring led to reduced internal resistance/charge transfer resistance due to the single crystalline nature of the nCu_2O mesosphere. Together, the excellent sensor performance combined with the use of low-cost green materials makes this a potentially valuable technology for applications where human and environmental exposure to mercury needs to be monitored, particularly in regions of the world where standard analytical techniques are inaccessible or cost-prohibitive.

ASSOCIATED CONTENT

Supporting Information

The Supporting Information is available free of charge on the ACS Publications website at DOI: 10.1021/acssuschemeng.8b02510.

Detailed list of materials and chemicals, detailed methods for nanoparticle preparation and electrochemical analysis, and supplementary figures (PDF)

AUTHOR INFORMATION

Corresponding Authors

*E-mail: sfoda20@hotmail.com.

*E-mail: emclamor@ufl.edu.

ORCID

S. M. Abdelbasir: 0000-0003-2698-2041

E. S. McLamore: 0000-0002-1662-7372

Notes

The authors declare no competing financial interest.

ACKNOWLEDGMENTS

The authors thank the National Science Foundation (ESM—grant no CBET-1511953, Nanobiosensing), the Agricultural and Biological Department graduate fellowship at the University of Florida (TVM), the Title VI grant from the University of Florida Center for Latin American Studies (ESM, IVT, DV), and the Colombian Department of Science Technology and Innovation — COLCIENCIAS (LMCH).

REFERENCES

(1) Demaio, A. R.; Rockström, J. Human and Planetary Health: Towards a Common Language. *Lancet* **2015**, *386*, e36—e37.

(2) Bernhoft, R. A. Mercury Toxicity and Treatment: A Review of the Literature. *J. Environ. Public Health* **2012**, *2012*, 1.

(3) Gibb, H.; O'Leary, K. G. Mercury Exposure and Health Impacts among Individuals in the Artisanal and Small-Scale Gold Mining Community: A Comprehensive Review. *Environ. Health Perspect.* **2014**, 667—672.

(4) Torres, A. D.; Rai, A. N.; Hardiek, M. L. Mercury Intoxication and Arterial Hypertension: Report of Two Patients and Review of the Literature. *Pediatrics* **2000**, *105* (3), E34.

(5) Vélez-Torres, I.; Vanegas, D. C.; McLamore, E. S.; Hurtado, D. Mercury Pollution and Artisanal Gold Mining in Alto Cauca, Colombia: Woman's Perception of Health and Environmental Impacts. *J. Environ. Dev.* **2018**, in press.

(6) Cui, X.; Fang, X.; Zhao, H.; Li, Z.; Ren, H. An Electrochemical Sensor for Dopamine Based on Polydopamine Modified Reduced Graphene Oxide Anchored with Tin Dioxide and Gold Nanoparticles. *Anal. Methods* **2017**, *9* (36), 5322—5332.

(7) Vanegas, D. C.; Taguchi, M.; Chaturvedi, P.; Burrs, S.; Tan, M.; Yamaguchi, H.; McLamore, E. S. A Comparative Study of Carbon—Platinum Hybrid Nanostructure Architecture for Amperometric Biosensing. *Analyst* **2014**, *139* (3), 660—667.

(8) He, Q.; Das, S. R.; Garland, N. T.; Jing, D.; Hondred, J. A.; Cargill, A. A.; Ding, S.; Karunakaran, C.; Claussen, J. C. Enabling Inkjet Printed Graphene for Ion Selective Electrodes with Post-Print Thermal Annealing. *ACS Appl. Mater. Interfaces* **2017**, *9*, 12719.

(9) Lin, J.; Peng, Z.; Liu, Y.; Ruiz-Zepeda, F.; Ye, R.; Samuel, E. L. G.; Yacaman, M. J.; Yakobson, B. I.; Tour, J. M. Laser-Induced Porous Graphene Films from Commercial Polymers. *Nat. Commun.* **2014**, *5*, 5714.

(10) El-Kady, M. F.; Strong, V.; Dubin, S.; Kaner, R. B. Laser Scribing of High-Performance and Flexible Graphene-Based Electrochemical Capacitors. *Science (Washington, DC, U. S.)* **2012**, *335* (6074), 1326—1330.

(11) Li, Y.; Luong, D. X.; Zhang, J.; Tarkunde, Y. R.; Kittrell, C.; Sargunaraj, F.; Ji, Y.; Arnusch, C. J.; Tour, J. M. Laser-Induced Graphene in Controlled Atmospheres: From Superhydrophilic to Superhydrophobic Surfaces. *Adv. Mater.* **2017**, *29* (27), 1700496.

(12) Duy, L. X.; Peng, Z.; Li, Y.; Zhang, J.; Ji, Y.; Tour, J. M. Laser-Induced Graphene Fibers. *Carbon* **2018**, *126*, 472—479.

(13) Wu, D.; Deng, L.; Mei, X.; Teh, K. S.; Cai, W.; Tan, Q.; Zhao, Y.; Wang, L.; Zhao, L.; Luo, G.; Sun, D.; Lin, L. Direct-Write Graphene Resistors on Aromatic Polyimide for Transparent Heating Glass. *Sens. Actuators, A* **2017**, *267*, 327—333.

(14) Vanegas, D. C.; Patiño, L.; Mendez, C.; de Oliveira, D. A.; Torres, A. M.; Gomes, C. L.; McLamore, E. S. Laser Scribed Graphene Biosensor for Detection of Biogenic Amines in Food Samples Using Locally Sourced Materials. *Biosensors* **2018**, *8* (2), 42.

(15) Geetha Bai, R.; Muthoosamy, K.; Zhou, M.; Ashokkumar, M.; Huang, N. M.; Manickam, S. Sonochemical and Sustainable Synthesis of Graphene-Gold (G-Au) Nanocomposites for Enzymeless and Selective Electrochemical Detection of Nitric Oxide. *Biosens. Bioelectron.* **2017**, *87*, 622—629.

(16) Paczosa-Bator, B.; Piech, R.; Wardak, C.; Cabaj, L. Application of Graphene Supporting Platinum Nanoparticles Layer in Electrochemical Sensors with Potentiometric and Voltammetric Detection. *Ionics* **2018**, *24*, 2455.

(17) Cincotto, F. H.; Golinelli, D. L. C.; Machado, S. A. S.; Moraes, F. C. Electrochemical Sensor Based on Reduced Graphene Oxide Modified with Palladium Nanoparticles for Determination of

DOI: 10.1021/acssuschemeng.8b02510
ACS Sustainable Chem. Eng. XXXX, XXX, XXX—XXX

Desipramine in Urine Samples. *Sens. Actuators, B* **2017**, *239*, 488–493.
(18) Daniele, M.; Pedrero, M.; Burrs, S.; Chaturvedi, P.; Wan Salim, W. W. A.; Kuralay, F.; Campuzano, S.; McLamore, E. S.; Claussen, J. C.; Cargill, A. A.; Ding, S. Chapter 11. Hybrid Metallic Nanoparticles: Enhanced Bioanalysis and Biosensing via Carbon Nanotubes, Graphene, and Organic Conjugation. *Nanobiosensors and Nanobioanalyses* **2015**, 137–166.
(19) Kiran Kumar, S. R.; Mamatha, G. P.; Muralidhara, H. B.; Anantha, M. S.; Yallappa, S.; Hungund, B. S.; Yogesh Kumar, K. Highly Efficient Multipurpose Graphene Oxide Embedded with Copper Oxide Nanohybrid for Electrochemical Sensors and Biomedical Applications. *J. Sci. Adv. Mater. Devices* **2017**, *2*, 493.
(20) Reddy, K. H. V.; Satish, G.; Ramesh, K.; Karnakar, K.; Nageswar, Y. V. D. An Efficient Synthesis of N-Substituted Indoles from Indoline/Indoline Carboxylic Acid via Aromatization Followed by C-N Cross-Coupling Reaction by Using Nano Copper Oxide as a Recyclable Catalyst. *Tetrahedron Lett.* **2012**, *53* (24), 3061–3065.
(21) Yang, B.; Mao, Z.; Zhu, X.; Wan, Y. Functionalised Chitosan as a Green, Recyclable, Supported Catalyst for the Copper-Catalysed. Ullmann C-N Coupling Reaction in Water. *Catal. Commun.* **2015**, *60*, 92–95.
(22) Gawande, M. B.; Goswami, A.; Felpin, F. X.; Asefa, T.; Huang, X.; Silva, R.; Zou, X.; Zboril, R.; Varma, R. S. Cu and Cu-Based Nanoparticles: Synthesis and Applications in Catalysis. *Chem. Rev.* **2016**, *116*, 3722–3811.
(23) Ben Aissa, M. A.; Tremblay, B.; Andrieux-Ledier, A.; Maisonhaute, E.; Raouafi, N.; Courty, A. Copper Nanoparticles of Well-Controlled Size and Shape: A New Advance in Synthesis and Self-Organization. *Nanoscale* **2015**, *7* (7), 3189–3195.
(24) Ng, C. H. B.; Fan, W. Y. Shape Evolution of Cu2O Nanostructures via Kinetic and Thermodynamic Controlled Growth. *J. Phys. Chem. B* **2006**, *110* (42), 20801–20807.
(25) Gou, L.; Murphy, C. J. Solution-Phase Synthesis of Cu2O Nanocubes. *Nano Lett.* **2003**, *3* (2), 231–234.
(26) Dong, Y.; Li, Y.; Wang, C.; Cui, A.; Deng, Z. Preparation of Cuprous Oxide Particles of Different Crystallinity. *J. Colloid Interface Sci.* **2001**, *243* (1), 85–89.
(27) Zhang, X.; Xie, Y.; Xu, F.; Liu, X.; Xu, D. Shape-Controlled Synthesis of Submicro-Sized Cuprous Oxide Octahedra. *Inorg. Chem. Commun.* **2003**, *6* (11), 1390–1392.
(28) Ahmed, A.; Gajbhiye, N. S.; Joshi, A. G. Low Cost, Surfactant-Less, One Pot Synthesis of Cu2O Nano-Octahedra at Room Temperature. *J. Solid State Chem.* **2011**, *184* (8), 2209–2214.
(29) Xiu, F. R.; Zhang, F. S. Size-Controlled Preparation of Cu2O Nanoparticles from Waste Printed Circuit Boards by Supercritical Water Combined with Electrokinetic Process. *J. Hazard. Mater.* **2012**, *233–234*, 200–206.
(30) Kim, D. S.; Kim, J. H.; Suematsu, H.; Tanaka, K.; Ryu, B. K. Synthesis of Sn–Bi–Cu Intermetallic Compound Nanoparticles by Pulsed Wire Discharge of Sn–Bi and Cu Wires. *J. Nanosci. Nanotechnol.* **2017**, *17* (10), 7714.
(31) Kim, J.; Kang, S. W.; Mun, S. H.; Kang, Y. S. Facile Synthesis of Copper Nanoparticles by Ionic Liquids and Its Application to Facilitated Olefin Transport Membranes. *Ind. Eng. Chem. Res.* **2009**, *48* (15), 7437–7441.
(32) Han, K. I.; Kang, S. W.; Kim, J.; Kang, Y. S. Effect of Ionic Liquids on Dissociation of Copper Flake into Copper Nanoparticles and Its Application to Facilitated Olefin Transport Membranes. *J. Membr. Sci.* **2011**, *374* (1–2), 43–48.
(33) Moghimi-Rad, J.; Zabihi, F.; Hadi, I.; Ebrahimi, S.; Isfahani, T. D.; Sabbaghzadeh, J. Effect of Ultrasound Radiation on the Size and Size Distribution of Synthesized Copper Particles. *J. Mater. Sci.* **2010**, *45* (14), 3804–3811.
(34) Shimotsuma, Y.; Yuasa, T.; Homma, H.; Sakakura, M.; Nakao, A.; Miura, K.; Hirao, K.; Kawasaki, M.; Qiu, J.; Kazansky, P. G. Photoconversion of Copper Flakes to Nanowires with Ultrashort Pulse Laser Irradiation. *Chem. Mater.* **2007**, *19* (6), 1206–1208.
(35) Sadrolhosseini, A. R.; Noor, A. S. B. M.; Shameli, K.; Mamdoohi, G.; Moksin, M. M.; Adzir Mahdi, M. Laser Ablation Synthesis and Optical Properties of Copper Nanoparticles. *J. Mater. Res.* **2013**, *28* (18), 2629–2636.
(36) Lu, C.; Qi, L.; Yang, J.; Wang, X.; Zhang, D.; Xie, J.; Ma, J. One-Pot Synthesis of Octahedral Cu2O Nanocages via a Catalytic Solution Route. *Adv. Mater.* **2005**, *17* (21), 2562–2567.
(37) Ma, L. L.; Li, J. L.; Sun, H. Z.; Qiu, M. Q.; Wang, J. B.; Chen, J. Y.; Yu, Y. Self-Assembled Cu2O Flowerlike Architecture: Polyol Synthesis, Photocatalytic Activity and Stability under Simulated Solar Light. *Mater. Res. Bull.* **2010**, *45* (8), 961–968.
(38) Majumdar, A.; Xu, H. Z.; Zhao, F.; Keay, J. C.; Jayasinghe, L.; Khosravani, S.; Lu, X.; Kelkar, V.; Shi, Z. Bandgap Energies and Refractive Indices of Pb1-XSrxSe. *J. Appl. Phys.* **2004**, *95* (3), 939–942.
(39) Vanegas, D. C.; Taguchi, M.; Chaturvedi, P.; Burrs, S.; Tan, M.; Yamaguchi, H.; McLamore, E. S. A Comparative Study of Carbon-Platinum Hybrid Nanostructure Architecture for Amperometric Biosensing. *Analyst* **2014**, *139* (3), 660–667.
(40) Chaturvedi, P.; Vanegas, D. C.; Taguchi, M.; Burrs, S. L.; Sharma, P.; McLamore, E. S. A Nanoceria-Platinum-Graphene Nanocomposite for Electrochemical Biosensing. *Biosens. Bioelectron.* **2014**, *58*, 179–185.
(41) Taguchi, M.; Schwalb, N.; Rong, Y.; Vanegas, D. C.; Garland, N.; Tan, M.; Yamaguchi, H.; Claussen, J. C.; McLamore, E. S. PulSED: Pulsed Sonoelectrodeposition of Fractal Nanoplatinum for Enhancing Amperometric Biosensor Performance. *Analyst* **2016**, *141*, 3367.
(42) Tehrani, F.; Bavarian, B. Facile and Scalable Disposable Sensor Based on Laser Engraved Graphene for Electrochemical Detection of Glucose. *Sci. Rep.* **2016**, *6* (1), 27975.
(43) Fenzl, C.; Nayak, P.; Hirsch, T.; Wolfbeis, O. S.; Alshareef, H. N.; Baeumner, A. J. Laser-Scribed Graphene Electrodes for Aptamer-Based Biosensing. *ACS Sensors* **2017**, *2* (5), 616–620.
(44) Vanegas, D. C.; Patiño, L.; Mendez, C.; de Oliveira, D. A.; Torres, A. M.; Gomes, C.; McLamore, E. S. Laser Scribed Graphene Biosensor for Detection of Biogenic Amines in Food Samples Using Locally Sourced Materials. *Biosensors* **2018**, *8* (2), 42–49.
(45) Fattahi, A.; Bahrololoom, M. E. Investigating the Effect of Magnetic Field on Pulse Electrodeposition of Magnetic and Non-Magnetic Nanostructured Metals. *Surf. Coat. Technol.* **2015**, *261*, 426–435.
(46) Lavagnini, I.; Antiochia, R.; Magno, F. An Extended Method for the Practical Evaluation of the Standard Rate Constant from Cyclic Voltammetric Data. *Electroanalysis* **2004**, *16* (6), 505–506.
(47) Chaturvedi, P.; Vanegas, D. C.; Hauser, B. A.; Foster, J. S.; Sepúlveda, M. S.; McLamore, E. S. Microprofiling Real Time Nitric Oxide Flux for Field Studies Using a Stratified Nanohybrid Carbon-Metal Electrode. *Anal. Methods* **2017**, *9* (42), 6061.
(48) Sotomayor, M. D. P. T.; Tanaka, A. A.; Kubota, L. T. Development of an Amperometric Sensor Highly Selective for Dopamine and Analogous Compounds Determination Using Bis-(2,29-Bipyridil) Copper(II)Chloride Complex. *Electroanalysis* **2003**, *15* (9), 787–796.
(49) Dai, X.; Compton, R. G. Detection of As(Iii) via Oxidation to As(v) Using Platinum Nanoparticle Modified Glassy Carbon Electrodes: Arsenic Detection without Interference from Copper. *Analyst* **2006**, *131* (4), 516.
(50) Gao, H.; Zhang, J.; Wang, M. Controllable Growth and Photocatalytic Activity of Cu2O Solid Microspheres. *Mater. Res. Bull.* **2013**, *48* (9), 3431–3437.
(51) Kumar, R.; Rai, P.; Sharma, A. Facile Synthesis of Cu2O Microstructures and Their Morphology Dependent Electrochemical Supercapacitor Properties. *RSC Adv.* **2016**, *6* (5), 3815–3822.
(52) Yuan, Z.; Zhang, Y.; Chen, H.; Xu, C. CTAB-Assisted Synthesis of Eight-Horn-Shaped Cu2O Crystals via a Simple Solution Approach. *J. Mater. Sci.: Mater. Electron.* **2018**, *29* (5), 4256–4260.

DOI: 10.1021/acssuschemeng.8b02510
ACS Sustainable Chem. Eng. XXXX, XXX, XXX–XXX

(53) Moores, A.; Goettmann, F. The Plasmon Band in Noble Metal Nanoparticles: An Introduction to Theory and Applications. *New J. Chem.* **2006**, *30* (8), 1121.
(54) Link, S.; El-Sayed, M. A. Shape and Size Dependence of Radiative, Non-Radiative and Photothermal Properties of Gold Nanocrystals. *Int. Rev. Phys. Chem.* **2000**, *19* (3), 409−453.
(55) Ito, T.; Yamaguchi, H.; Okabe, K.; Masumi, T. Single-Crystal Growth and Characterization of Cu2O and CuO. *J. Mater. Sci.* **1998**, *33*, 3555−3566.
(56) Gu, Q.; Wang, B. Correlation between Structural Defects and Optical Properties of Cu2O Nanowires Grown by Thermal Oxidation. *Wire* **2010**, *12*, arXiv:1012.5338..
(57) Wang, Y.; Miska, P.; Pilloud, D.; Horwat, D.; Mücklich, F.; Pierson, J. F. Transmittance Enhancement and Optical Band Gap Widening of Cu2O Thin Films after Air Annealing. *J. Appl. Phys.* **2014**, *115* (7), 073505.
(58) Shih, P. H.; Ji, J. Y.; Ma, Y. R.; Wu, S. Y. Size Effect of Surface Magnetic Anisotropy in Cu_2O Nanoparticles. *J. Appl. Phys.* **2008**, *103* (7), 07B735.
(59) Chen, C.; He, L.; Lai, L.; Zhang, H.; Lu, J.; Guo, L.; Li, Y. Magnetic Properties of Undoped Cu_2O Fine Powders with Magnetic Impurities and/or Cation Vacancies. *J. Phys.: Condens. Matter* **2009**, *21* (14), 145601.
(60) Harbola, M. K.; Sahni, V. Structure of the Fermi Hole at Surfaces. *Phys. Rev. B: Condens. Matter Mater. Phys.* **1988**, *37* (2), 745−754.
(61) Manousakis, E. The Spin- Heisenberg Antiferromagnet on a Square Lattice and Its Application to the Cuprous Oxides. *Rev. Mod. Phys.* **1991**, *63* (1), 1−62.
(62) Sundaresan, A.; Rao, C. N. R. Ferromagnetism as a Universal Feature of Inorganic Nanoparticles. *Nano Today* **2009**, *4*, 96−106.
(63) Bellunato, A.; Arjmandi Tash, H.; Cesa, Y.; Schneider, G. F. Chemistry at the Edge of Graphene. *ChemPhysChem* **2016**, *17*, 785−801.
(64) Yuan, W.; Zhou, Y.; Li, Y.; Li, C.; Peng, H.; Zhang, J.; Liu, Z.; Dai, L.; Shi, G. The Edge- and Basal-Plane-Specific Electrochemistry of a Single-Layer Graphene Sheet. *Sci. Rep.* **2013**, *3* (1), 2248.
(65) McLamore, E. S.; Convertino, M.; Ocsoy, I.; Vanegas, D. C.; Taguchi, M.; Rong, Y.; Gomes, C.; Chaturvedi, P.; Claussen, J. C. Biomimetic Fractal Nanometals as a Transducer Layer in Electrochemical Biosensing. *Semiconductor Device-Based Sensors for Gas, Chemical, and Biomedical Applications* **2016**, 35−69.
(66) Marr, K. M.; Chen, B.; Mootz, E. J.; Geder, J.; Pruessner, M.; Melde, B. J.; Vanfleet, R. R.; Medintz, I. L.; Iverson, B. D.; Claussen, J. C. High Aspect Ratio Carbon Nanotube Membranes Decorated with Pt Nanoparticle Urchins for Micro Underwater Vehicle Propulsion via H2O2 Decomposition. *ACS Nano* **2015**, *9* (8), 7791−7803.
(67) Claussen, J. C.; Daniele, M. A.; Geder, J.; Pruessner, M.; Mäkinen, A. J.; Melde, B. J.; Twigg, M.; Verbarg, J. M.; Medintz, I. L. Platinum-Paper Micromotors: An Urchin-like Nanohybrid Catalyst for Green Monopropellant Bubble-Thrusters. *ACS Appl. Mater. Interfaces* **2014**, *6* (20), 17837−17847.
(68) Zhou, Q.; Wang, B.; Wang, P.; Dellago, C.; Wang, Y.; Fang, Y. Nanoparticle-Based Crystal Growth via Multistep Self-Assembly. *CrystEngComm* **2013**, *15* (25), 5114.
(69) Alonso, F.; Moglie, Y.; Radivoy, G.; Yus, M. Multicomponent Synthesis of 1,2,3-Triazoles in Water Catalyzed by Copper Nanoparticles on Activated Carbon. *Adv. Synth. Catal.* **2010**, *352* (18), 3208−3214.
(70) Alonso, F.; Moglie, Y.; Radivoy, G.; Yus, M. Alkenes as Azido Precursors for the One-Pot Synthesis of 1,2,3-Triazoles Catalyzed by Copper Nanoparticles on Activated Carbon. *J. Org. Chem.* **2013**, *78* (10), 5031−5037.
(71) Georgakilas, V.; Gournis, D.; Tzitzios, V.; Pasquato, L.; Guldi, D. M.; Prato, M. Decorating Carbon Nanotubes with Metal or Semiconductor Nanoparticles. *J. Mater. Chem.* **2007**, *17* (26), 2679.
(72) Mondal, P.; Sinha, A.; Salam, N.; Roy, A. S.; Jana, N. R.; Islam, S. M. Enhanced Catalytic Performance by Copper Nanoparticle−Graphene Based Composite. *RSC Adv.* **2013**, *3* (16), 5615.
(73) Luo, J.; Jiang, S.; Zhang, H.; Jiang, J.; Liu, X. A Novel Non-Enzymatic Glucose Sensor Based on Cu Nanoparticle Modified Graphene Sheets Electrode. *Anal. Chim. Acta* **2012**, *709*, 47−53.
(74) Gu, J. D.; Mitton, D. B.; Ford, T. E.; Mitchell, R. Microbial Degradation of Polymeric Coatings Measured by Electrochemical Impedance Spectroscopy. *Biodegradation* **1998**, *9* (1), 39−45.
(75) Gu, J. D. Microbial Colonization of Polymeric Materials for Space Applications and Mechanisms of Biodeterioration: A Review. *Int. Biodeterior. Biodegrad.* **2007**, *59* (3), 170−179.
(76) Min, K.; Yoo, Y. J. Amperometric Detection of Dopamine Based on Tyrosinase-SWNTs-Ppy Composite Electrode. *Talanta* **2009**, *80* (2), 1007−1011.
(77) Tembe, S.; Karve, M.; Inamdar, S.; Haram, S.; Melo, J.; D'Souza, S. F. Development of Electrochemical Biosensor Based on Tyrosinase Immobilized in Composite Biopolymeric Film. *Anal. Biochem.* **2006**, *349* (1), 72−77.
(78) Njagi, J.; Chernov, M. M.; Leiter, J. C.; Andreescu, S. Amperometric Detection of Dopamine in Vivo with an Enzyme Based Carbon Fiber Microbiosensor. *Anal. Chem.* **2010**, *82* (3), 989−996.
(79) Sharma, V. V.; Tonelli, D.; Guadagnini, L.; Gazzano, M. Copper-Cobalt Hexacyanoferrate Modified Glassy Carbon Electrode for an Indirect Electrochemical Determination of Mercury. *Sens. Actuators, B* **2017**, *238*, 9−15.
(80) Chaiyo, S.; Chailapakul, O.; Siangproh, W. Highly Sensitive Determination of Mercury Using Copper Enhancer by Diamond Electrode Coupled with Sequential Injection-Anodic Stripping Voltammetry. *Anal. Chim. Acta* **2014**, *852*, 55−62.
(81) Mohammadi, H.; Amine, A.; El Rhazi, M.; Brett, C. M. A. Copper-Modified Gold Electrode Specific for Monosaccharide Detection: Use in Amperometric Determination of Phenylmercury Based on Invertase Enzyme Inhibition. *Talanta* **2004**, *62* (5), 951−958.
(82) Yang, H.; Kannappan, S.; Pandian, A. S.; Jang, J.-H.; Lee, Y. S.; Lu, W. Graphene Supercapacitor with Both High Power and Energy Density. *Nanotechnology* **2017**, *28* (44), 445401.
(83) Jang, H.; Park, Y. J.; Chen, X.; Das, T.; Kim, M. S.; Ahn, J. H. Graphene-Based Flexible and Stretchable Electronics. *Adv. Mater.* **2016**, *28* (22), 4184−4202.
(84) Hossain, M. N.; Wen, J.; Chen, A. Unique Copper and Reduced Graphene Oxide Nanocomposite toward the Efficient Electrochemical Reduction of Carbon Dioxide. *Sci. Rep.* **2017**, *7* (1), 3184.
(85) Das, S. R.; Nian, Q.; Cargill, A. A.; Hondred, J. A.; Ding, S.; Saei, M.; Cheng, G. J.; Claussen, J. C. 3D Nanostructured Inkjet Printed Graphene via UV-Pulsed Laser Irradiation Enables Paper-Based Electronics and Electrochemical Devices. *Nanoscale* **2016**, *8* (35), 15870−15879.
(86) Huang, X.; Leng, T.; Zhu, M.; Zhang, X.; Chen, J.; Chang, K.; Aqeeli, M.; Geim, A. K.; Novoselov, K. S.; Hu, Z. Highly Flexible and Conductive Printed Graphene for Wireless Wearable Communications Applications. *Sci. Rep.* **2016**, *5*, 18298.
(87) Fu, K.; Wang, Y.; Yan, C.; Yao, Y.; Chen, Y.; Dai, J.; Lacey, S.; Wang, Y.; Wan, J.; Li, T.; et al. Graphene Oxide-Based Electrode Inks for 3D-Printed Lithium-Ion Batteries. *Adv. Mater.* **2016**, *28* (13), 2587−2594.

DOI: 10.1021/acssuschemeng.8b02510
ACS Sustainable Chem. Eng. XXXX, XXX, XXX−XXX